Spectral Ship Surveillance from Space

A. Schaum, Eric Allman, Robert A. Leathers
Naval Research Laboratory,
Washington, D.C. 20375-5320
Matthew Stites
Space Dynamics Laboratory
Logan, Utah 84341

Abstract- Remote surveillance of the ocean will soon become a high priority for the U.S. Navy, as international threats to close strategic choke points intensify, as piracy flourishes, and as gaps in U.S. waters continue to permit illegal intrusions with contraband cargo. A critical need is arising to identify threats as early and as distant from our shores as possible. A growing constellation of spectrally-capable satellites can facilitate this function, which must be performed autonomously. Earth's total ocean area is 10^{14} (1 m)^2 pixels. This paper develops a spectral anomaly detection algorithm that is based on a statistical mixture model of clouds and ocean. A real time implementable prototype version is derived using clairvoyant fusion methods. Development of a second generation version applicable to a more accurate clutter model is also described.
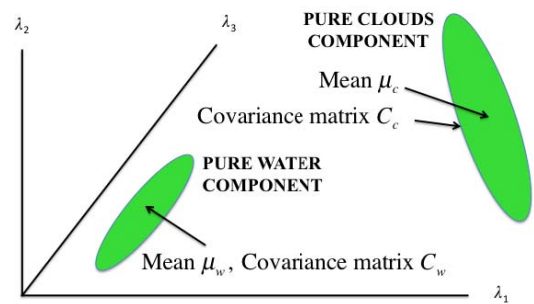
I. BACKGROUND

The aim of the research we describe is to produce a fully autonomous detection algorithm, based primarily on multispectral electro-optical data, which can detect seagoing vessels from an overhead platform. Detections are defined as spectral anomalies; no prior target signature information is assumed. The need for absolute radiometric sensor calibration is to be avoided. And we seek a closed form detection algorithm with at most one free parameter, to allow exercising the tradeoff between false alarm and detection probabilities. We describe a work in progress, with encouraging preliminary results using a prototype detector, along with data interpretations suggesting future algorithm enhancements.

II. COMPOSITE ANOMALY DETECTION

Fig. 1 depicts geometrically the distributions in a spectral feature space of the two principal pure background components encountered by an overhead surveillance asset pointed at the ocean; ocean water and clouds. Our analysis assumes that large areas of the pure versions of either component have been identified in a scene, based generally on the fact that the ocean looks much darker in longer wavelengths than clouds. From these partial segmentations of a scene (typically with ~ 50 million pixels) the first- and second-order multivariate statistics of each segment are sampled and stored. These are the spectral means and covariance matrices of each segment.

Fig. 1. The clutter declaration region (green) for an anomaly detector for a two-component background model is the union of those for the one-component problems.

We assume further that each distribution is sufficiently well described with a multivariate Gaussian probability density function (pdf). The ellipsoids of Fig. 1 represent surfaces of constant pdf, with each principal axis two standard deviations long in the corresponding data direction.

Anomaly detection for each segment alone consists of thresholding its pdf. On the other hand, if either segment can be present, the natural extension for anomaly detection requires that both anomaly detectors give positive results. This is equivalent to fusing their "background declaration" regions, i.e., forming their set-theoretic union. Operationally, this is equivalent to logically ANDing the two detector decisions.

Setting a detection threshold corresponds to defining the scale of the ellipsoid used in an anomaly detector, and the thresholds can differ when two (or more) anomaly detectors are fused. For example, if the ellipsoids are constrained to enclose the same total probability, the composite anomaly detector is said to result from "CFAR fusion" [1]. Each individual detector, if applied to the corresponding pure clutter distribution, would produce the same false alarm probability. For Gaussian distributions, CFAR fusion is also

equivalent to constraining both ellipsoids to correspond to the same number of standard deviations.

The actual composite anomaly detection problem must include all possible fractional mixtures of cloud and ocean, as in Fig. 2. The allowed fractions f are infinite in number, and so ANDing all relevant anomaly detectors is infeasible.

**TWO-COMPONENT MIXTURE MODEL
GLRT-BASED ANOMALY DETECTION**
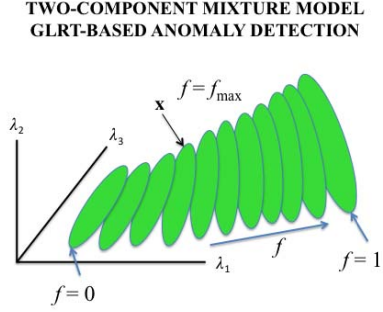
Fig. 2. For each sample feature vector x, the GLRT selects the most likely mixture realization and uses the corresponding pdf (Equation 1) to estimate anomalousness.

The most common approach for dealing with such composite hypothesis testing problems is to resort to the generalized likelihood ratio test (GLRT). For anomaly detection, this means solving the maximization problem

$$d_{GLRT}(\mathbf{x}) = \frac{1}{\underset{f}{Max}\left(p_f(\mathbf{x})\right)} - T, \qquad (1)$$

where T is an adjustable threshold. Generally any detection algorithm can be described by a discriminant function d. Positive values of d indicate that sample spectrum $\mathbf{x}$ is to be declared a positive detection, in the present case, an anomaly. The pdf of a mixture

$$p_f(\mathbf{x}) = \frac{1}{\left(\sqrt{2\pi}\right)^N \left\|C(f)\right\|^{1/2}} \exp\left[-\frac{1}{2}\left(\mathbf{x} - \mu_f\right)^f C^{-1}(f)\left(\mathbf{x} - \mu_f\right)\right] \quad (2)$$

describes the distribution of spectra for pixels containing a fraction f of cloud mixed with $(1-f)$ of ocean (see Fig. 1). The mixed means and covariance matrices are given by:

$$\mu_f = (1-f)\mu_w + f\mu_c, \quad C(f) = (1-f)^{p_w} C_w + f^{p_c} C_c. \quad (3)$$

The subscripts w and c refer to water and cloud respectively. A p–value of one corresponds to a spatial/spectral model with zero-correlation length (in practice, extremely sub-pixel) and the value two corresponds to infinite (in practice,

multi-pixel) correlation length [2, 3]. These values may differ for water and cloud models. (Or be appropriate for neither.) The detection algorithms discussed in this paper are insensitive to the assumed p-values.

The mathematics of the detection problem is greatly simplified if all the data is first subjected to a whitening operation. And so we transform every pixel according to

$$\mathbf{x} \to C_w^{-\frac{1}{2}}\left(\mathbf{x} - \mu_w\right). \qquad (4)$$

This makes the mean of the pure water pixels zero and their covariance matrix equal to the identity matrix. Therefore, the whitened space version of Equations (3) is

$$\mu_f = f\mu_c, \quad C(f) = (1-f)^{p_w} I + f^{p_c} C_c, \qquad (5)$$

with I the identity matrix, and C_c the whitened version of the cloud covariance matrix. (The C_c in (3) is transformed according to $C_c \to C_w^{-\frac{1}{2}} C_c C_w^{-\frac{1}{2}}$.)

However, these simplifications still do not allow a closed form solution to equation (1).

One way to move closer to such a solution involves: (1) simplifying the clutter model and (2) abandoning the GLRT in favor of the fusion approach. For example, if the pure water and pure cloud covariance matrices were scaled versions of each other, then in whitened space, the two pure distributions in Fig. 2 become the extreme two spherical ones in Fig. 3.
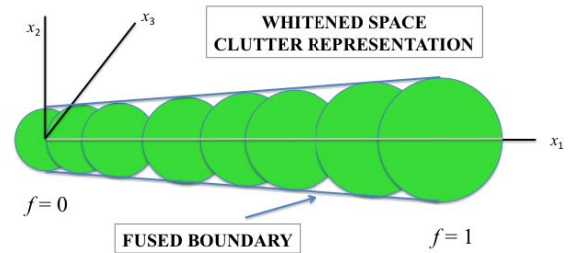
Fig. 3. Simplified composite clutter model. If pure water and pure cloud covariance matrices are scaled versions of each other, all clairvoyant anomaly detectors are spherical. Their thresholds can be varied with f to achieve a variety of envelope shapes, the simplest having a truncated conical boundary with spherical end caps.

Furthermore, C_c becomes proportional to I, as does $C(f)$, and so the anomaly detector (called a *clairvoyant*) for each value of f is a sphere, regardless of the assumed p values. The radius of each clairvoyant depends on the assumed threshold and can be adjusted to produce, for example, a linear dependence on the fraction f. In this case the detection boundary for the union of all the clairvoyants' clutter decla-

ration regions can be derived geometrically. It is a truncated hypercone with spherical end caps. This constitutes our prototype fused detector. It depends on two parameters, the slope and vertex of the enveloping cone. The availability of a geometrical solution to this fusion problem obviates the need to implement and AND an infinite number of detectors.

The rotational symmetry of the model about the *mean axis* (the horizontal line joining the pure clutter means in whitened space) admits a folded subspace representation [4] of the data. All data points in the N-dimensional feature space are rotated about the axis and placed in the upper half plane. Thus the Fig. 4 image appears in spectral space as the insert in Fig 5. If the data are also partitioned horizontally by color, as shown, the corresponding pixels in the spatial domain confirm the mixture model: Pure clouds in the central regions of cloud banks and increasingly mixed pixels approaching the edges. (The region of the image corresponding to the white part of the spectral plot has not been recolored.)


Fig. 4. RGB image derived from the Worldview-2 sensor. The high resolution panchromatic data has been colorized with a standard band-sharpening algorithm.
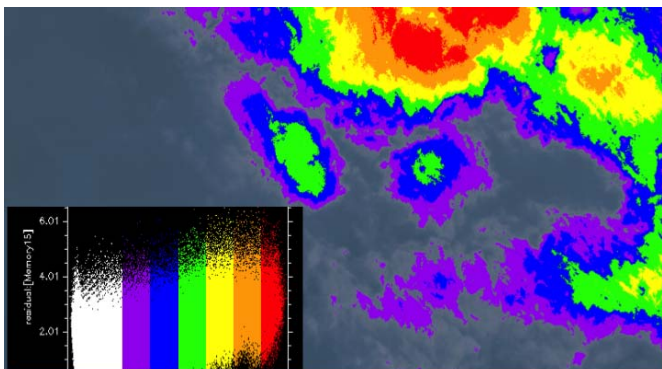

Fig. 5. Folded representation (inset) of spectral content of the image colored to reflect different water/cloud mixtures. Rightmost (red) pixels correspond to purest clouds. (Points colored white are left unchanged in image.)

The folded decision boundary is a straight line (with semicircular end caps), and to meet the final requirement that the detector depend on at most one parameter, we consider only horizontal lines. (In effect, both pure components are modeled with identical covariance matrices.) Thus, the upper left rectangle (expanded in Fig. 8) in the 50 million pixel image of Fig. 6 (from which pure water and pure cloud statistics were derived) corresponds to the folded representation of data (and detector) in Fig. 7.
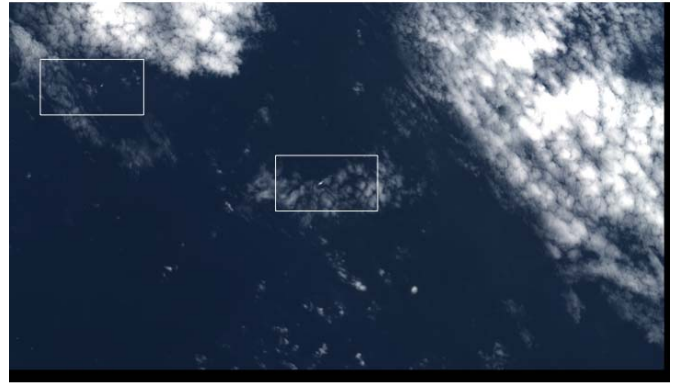
Fig. 6. RGB band sharpened image (9216 x 5120) pixels. Rectangular chips analyzed in Figures 7 through 12 with four legacy WorldView 2 bands (B,G,R,NIR).
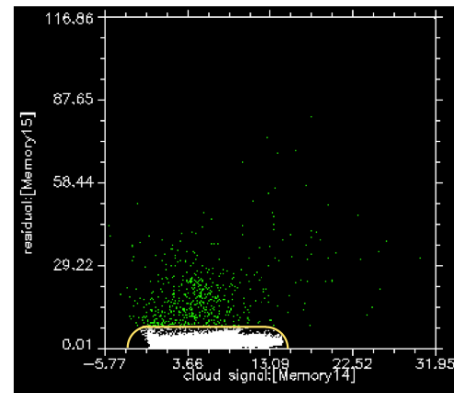
Fig. 7. Folded subspace representation of data (upper left rectangle of Fig. 6) and algorithm decision boundary (yellow). Detections (green) also appear in Fig. 8.

Fig. 9 shows a composite derived from the center rectangular region of Fig. 6. Notice the smaller less obvious vessel also detected (upper right corner). Shape-based panchromatic ATR methods experience high false alarm rates in such cloudy backgrounds.

Fig. 10 shows a higher resolution chip from the more prominent detection in Fig. 9. The beam and length of the vessel are easily estimated (from a digitally zoomed version of the picture) enabling its identification as an Australian-made High Speed Vessel (HSV).

Fig. 8. RGB image chip with threshold exceedances in green. Ship and wake are detected as anomalous to the water/cloud mixture model.
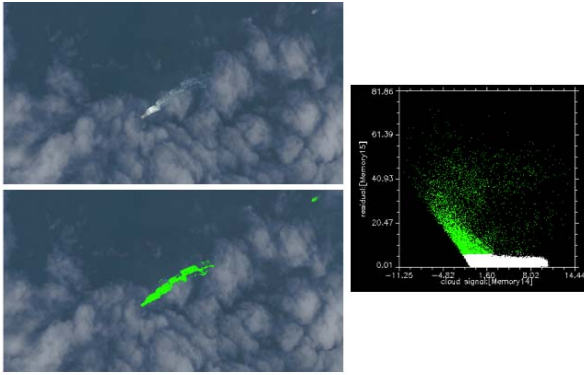

Fig. 9. Vessels detected under clouds between Honshu and Ooshima, Japan. From center rectangle in Fig. 6.


Fig. 10. High resolution (~ 1m GSD) band-sharpened pan image enables mensuration and identification.

Fig. 11 colorizes different parts of the folded scatterplot for interpretation in the image domain (Fig. 12). One possible explanation: If the wake pixels (actually jets of water from

the HSV's four engines) are primarily confined, in whitened (or radiance) space, to a hyperplane that is penetrated by the mean line (x-axis), the folding operation should place them in successive bands displaced from the left-hand linear feature in Fig. 11. This bodes well for extending the one-dimensional water/cloud subspace model used here, to include another subspace describing whitecaps. This would expand the detection methodology to allow detection not only in mixed water/cloud images, but also in the presence of high sea states.
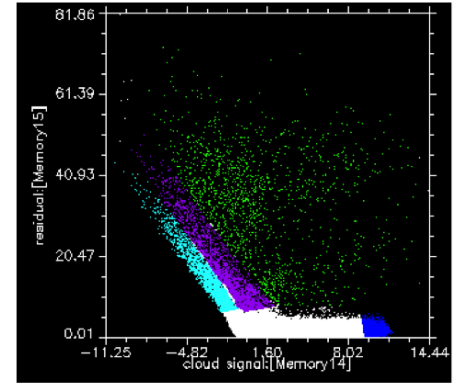
Fig. 11. Segmented scatterplot from Fig. 9. The technique helps with interpretation in the spatial domain (Fig. 12).
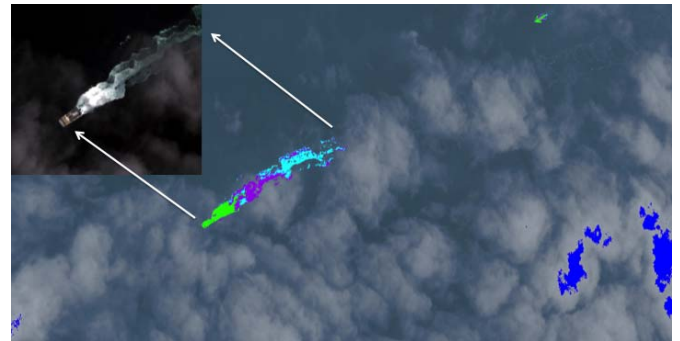
Fig. 12. Spatial/spectral correspondences. Dark blue pixels reconfirm the clutter model (see Fig 11). Light blue and purple pixels are different parts of HSV wake. Their distribution suggests that whitecaps lie in a linear subspace (pre-folding).

III. FUTURE

Now we discuss the next steps we are pursuing to evolve the prototype detector into a more capable Spectral Ship Surveillance (S3) algorithm.

A. Using a better clutter model: The S3 detector

A comparison of the pure water and pure cloud distributions in Fig. 13 shows that cloud variability can be consider-

ably different from that of the ocean. Thus, the original conical detector of Fig. 3 might need revisiting. However, the folded representation of Fig. 13 masks the directionality of this variability, which can differ by an order of magnitude in different directions within the three dimensions perpendicular to the (horizontal) mean axis. This violates the (whitened space) isotropy assumption for pure clouds in the simple prototype model described above.

Fig. 14(a) shows a more accurate clutter model (in whitened space) reflecting the anisotropies. In all of Fig. 14, green surfaces represent pdfs, yellow and red ones are clairvoyants' decision boundaries, and the magenta surface is (the bottom half of) the final closed form S3 decision boundary.
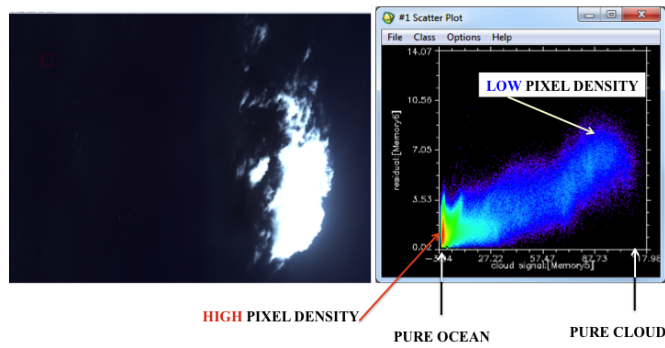
Fig. 13. Cloud spectral radiances can be more variable and anisotropic than ocean radiances. (Colors now refer to density of pixels.)

In this enhanced model, the covariance matrix of the pure cloud component is estimated from the data and is used in place of a scaled version of the pure water matrix, which appeared in the prototype described above. The coordinate system in Fig. 14(a) has been chosen to coincide with the principal component (PC) directions of the whitened cloud clutter, and because the water distribution is spherically symmetric, the same directions can serve as its PCs. Unfortunately, this choice of coordinates is still insufficient to allow a closed form solution.

Reference [5] describes how an approximate solution to this problem can be produced. The paper constructs an "effective" covariance matrix that replaces the C_c of Fig. 14, and which has the property that the mean line coincides with one of the PC axes, as illustrated in Fig. 14(b). That paper also shows how the fused surface can be constructed by gluing together "hyperstrings," one for each value of the mixing fraction f. That construction follows from the analytical formulation of the fusion principle
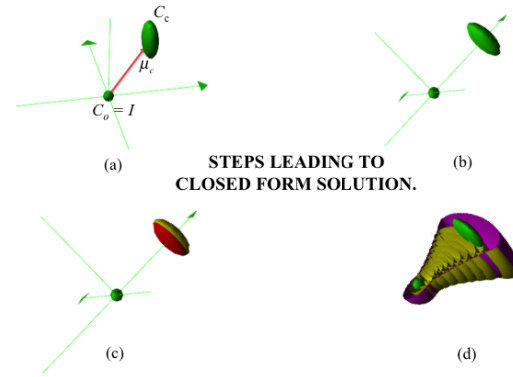
$$d_{FUSED}(\mathbf{x}) = \underset{f}{Min}\left[d_f(\mathbf{x})\right] = \underset{f}{Min}\left[\frac{1}{(p_f(\mathbf{x}))} - T_f\right]. \quad (6)$$

The *Min* operation demands the differential condition

$$d_{f+df}(\mathbf{x}) - d_f(\mathbf{x}) = 0, \quad (7)$$

whereas the equation describing the clairvoyant decision boundaries is

$$d_f(\mathbf{x}) = 0 . \quad (8)$$

Fig. 14. General problem (a) is simplified by use of "effective" covariance matrix for clouds (b). Hyperstrings (c) butted together construct solution (d).

Requiring that both equations (7) and (8) be satisfied means that the intersection of the two surfaces they define– the hyperstring–contributes to the fused decision boundary. That is, each hyperstring is the intersections of a pair of neighboring (infinitesimally close) clairvoyant decision boundaries, defined by (8) and $d_{f+df}(\mathbf{x}) = 0$. Two of these are depicted in Fig. 14(c).

Fig. 14 (d) plots an approximate closed form solution (magenta) to the fused detection problem consisting of glued hyperstrings for all values of f. This "S3" detector's boundary (where $d_{S3} = 0$) has been sliced in half to reveal the two pure clutter distributions (green) that generate it, along with a finite subset of the clairvoyant (yellow) detectors whose envelope is the exact detector. This geometrical comparison makes a strong case for this approximation approach.

Preliminary applications to data are encouraging. Fig. 15 exercises d_{S3} on WV-2 imagery. It shows that, because S3 uses a more accurate model of clouds, they are more readily suppressed in the search for anomalies.
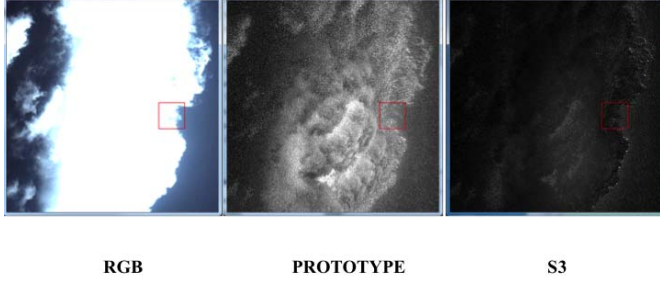
Fig. 15. The more accurate clutter model associated with the S3 detector suppresses clouds better than the prototype algorithm.

B. Twisted subspaces

The S3 detector and the clutter model that underlies it both lack the rotational invariance about the mean axis that characterizes the simpler prototype detector and model described earlier. Therefore, a folded subspace is not a faithful representation of the relationship between clutter and detection boundary.

We need to consider a more general form of mapping

$$F(x,\mathbf{y}) = (x, r(x,\mathbf{y})) \tag{9}$$

from the whitened space to the kind of 1½-dimensional visualization tool that works for symmetrical problems. We call this a twisted subspace.

We require the mapping r to be constant on any S3 decision boundary (making it faithful to the detection algorithm); we require further that it reduce to ordinary folding $(r(x,\mathbf{y}) \to \mathbf{y}^2)$ for rotationally symmetric problems.

These requirements do not uniquely determine the form of the twisted representation. The utility of several candidates is being examined.

C. A wake subspace?

The discussion surrounding Figs. 11 and 12 suggests that wake pixels tend to lie in some linear subspace of the N-dimensions sampled by the multispectral sensor. If this proves true for whitecaps as well, then any such pixels would be declared anomalous by both the prototype and S3 detectors. To extend S3 performance to high sea states, it might become necessary to expand the one-dimensional clutter model (along the water/cloud mean axis) to include another subspace to account for whitecaps. Defining the subspace in a consistent way is the subject of future research.

D. Dual fraction model

All the spectral data shown so far in this paper were derived from one of the two WV-2 spectrometers (see Fig. 16). Each spectrometer collects three visible and one near infrared channel. The legacy spectrometer collects nearly identical wavebands as the earlier 4-band QuickBird system.

The newer spectrometer typically collects data at the same location at sea-level as the legacy, but with a ½ second delay. This is accounted for in the pixel registration process. However, this mathematical registration fails both for moving objects and for high clouds, because of parallax effects. Thus, if all eight bands are used in the S3 detector, false anomalies can appear at cloud edges or wherever spatial gradients are high, such as in the brighter interior regions of clouds. Fig. 17 illustrates the effect, which is produced largely by horizontal gradients. These false alarms arise because the sensor data associated with them are alien to the clutter model, which assumes that only one mixing fraction occurs in any 8-band pixel.
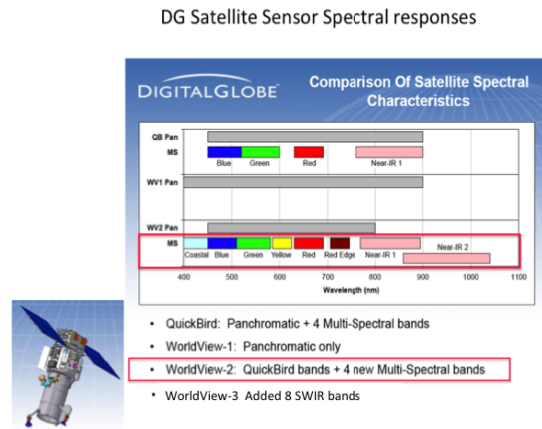
**Fig. 16. DigitalGlobe's satellite suite.**

Detection advantages should accrue to using the full 8-band system, because the newer four bands not only expand the range of spectral coverage beyond the QuickBird capabilities; two of the new bands are interleaved with the old. One expects extra correlations in these bands to reveal that what is nominally 8-dimensional clutter data is in fact confined to a lower-dimensional subspace. This effect is the primary mechanism explaining the power of hyperspectral systems to perform both signature-based and anomaly detection [5].

To overcome the problem of false alarms from misregistration, we are developing a sensor-specific detection model, featuring two independent mixing fractions, instead of the solitary f described above for S3. Each fraction applies to a different spectrometer, and the one-dimensional space (a line segment along the mean axis) of S3 is replaced by a two-dimensional parallelogram-shaped region to describe clutter

mixtures. We expect that the degradation in performance associated with this artificial clutter subspace will be more than offset by the gain associated with the extra correlations inherent to the 8-band data.
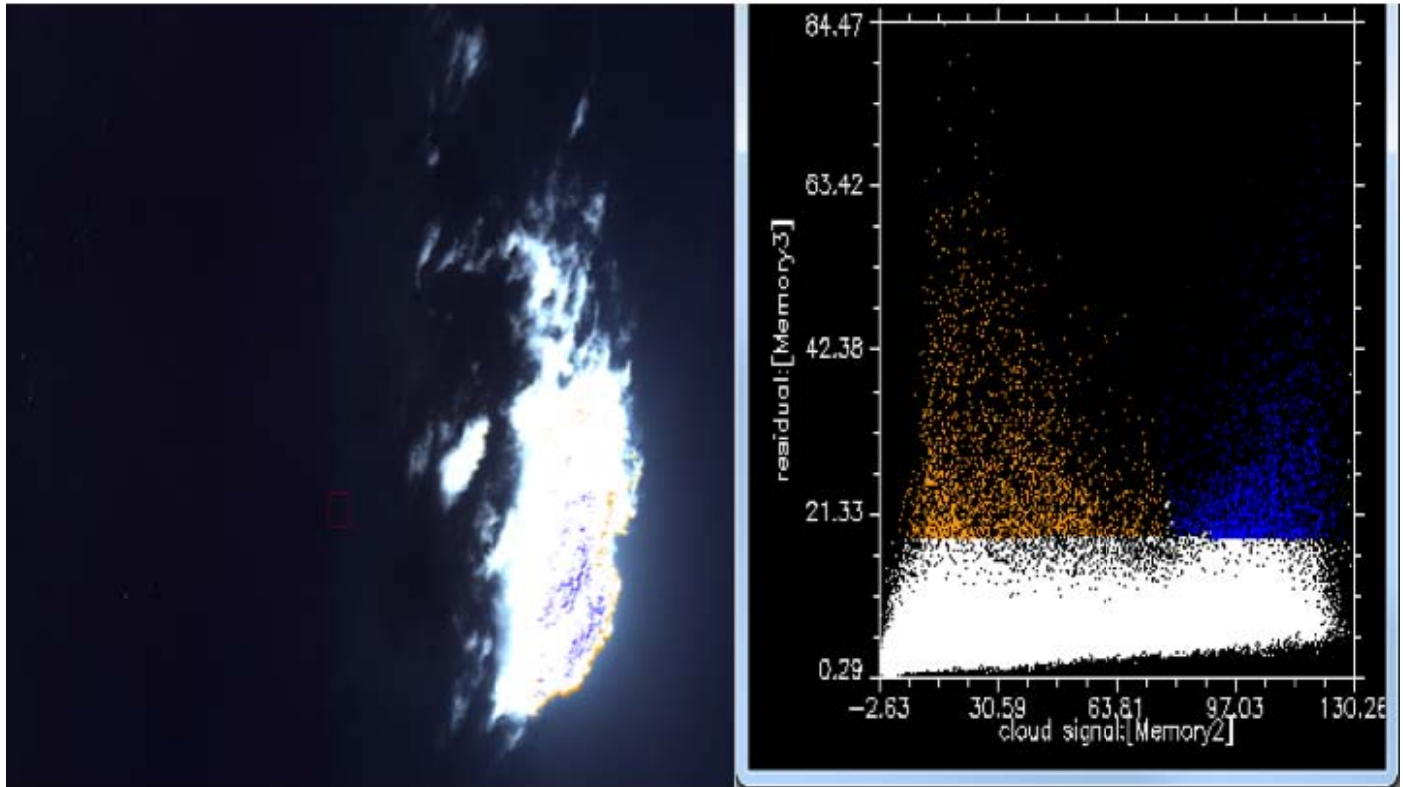
Fig. 17. Eight-band data. Misregistration between the two four-band spectrometers in the WorldView-2 sensor is not accounted for in the prototype anomaly detection algorithm, which can produce false alarms in the sensor scanning direction near strong image gradients.

E. Operational issues

Miscellaneous issues to be considered in future work.

1. Automatic threshold selection: Ideally an operational systems will require no human feedback to determine the proper threshold (e.g. the height of the horizontal line in Fig. 7). This will probably entail modeling the tails of clutter distributions after passing through S3.
2. Local vs. global statistics: The more accurate clutter model used in S3 might be unnecessary or even detrimental to detection in regions without bright clouds. The rectangular regions in Fig. 6 might be better suited for calculating background statistics than the entire 50-million pixel image.
3. Signature-based tracking. Once an anomaly has been detected, its spectral signature can be captured for use in future detection. Also, at the resolution of WV-2, many pix-

els typically lie on an ocean-going vessel, so that detection based on the statistics of target spectral pixels might be feasible.

IV. SUMMARY

This paper demonstrates the feasibility of space-based multispectral detection of anomalies at sea, based on a simple model of mixed water and cloud pixels. Potential deficiencies in the prototype algorithm have been identified, and a method for a producing a closed form detection algorithm that incorporates a more accurate clutter model have been found and are currently in testing. Future issues have also been identified on the path to creating a fully autonomous system that can operate effectively for a variety of sea states.

REFERENCES

[1] A. Schaum, Continuum Fusion, a theory of inference, with applications to hyperspectral detection, Opt. Express **18** Issue 8, pp. 8171-8181, 12 (2010).

[2] Alan Schaum, Continuum fusion solutions for replacement-target models in electro-optic detection, Applied Optics Vol. 53, Iss. 13, pp. C25–C31 (2014).

[3] Alan Schaum, Continuum Fusion Versions of the Finite Target Matched Filter for Sub-Pixel Detection, Proc. 5th IEEE International Geoscience and Remote Sensing Systems WHISPERS conference, 2013.

[4] Alan P. Schaum and Brian J. Daniel, Continuum fusion methods of spectral detection, Opt. Eng. 51, 111718 (July 10, 2012).

[5] Alan Schaum, Theoretical foundations of NRL spectral target detection algorithms, Applied Optics, November 1, 2015.